3. METHODOLOGY

3.1. SAMPLE PREPARATION AND APERTURE REPRESENTATION

The test results on aperture evolution came from the experimental studies performed by Fardin (2003) and the main techniques of sample preparation and aperture representation techniques developed in Fardin (2003) are described below, as well as the techniques used by Koyama *et al.* (2005) for measuring the aperture distribution during shearing.

A 250x250 mm sample of a natural rock fracture that comes from a quarry in Töre (North-eastern Sweden), firstly used by Lindfords in his Licentiate Thesis (1996), was used as a model of a rough rock fracture. This sample was also used as the parent fracture sample to cast various concrete fracture replicas of different sizes to study the effect of scale on the morphology, mechanics and transmissivity of single rock fractures (Fardin, 2003). As far as the rock fracture surfaces are concerned, they were measured by a 3D-laser scanner.

The rock fracture characterization is of crucial importance for the success of the investigation. This characterization was carried out according to the digital surface topography method (Hakami *et al*., 1995), with the aid of a 3D-laser scanner with a step size, i.e. distance between points in two parallel scanned lines, of 0.2 mm, and an accuracy of 20 μm. The laser sensor is a Kréon KLS 50, manufactured by Kréon Industrie, France, and it belongs to the Department of Land and Water Resources Engineering at the KTH (Royal Institute of Technology, Sweden). The characteristics of this device, which were explained in detail in Lanaro (2001), ensure the reliability of the collected data. As for the method of aperture measurement, the method described in Lanaro (2001) was used. This method mainly consists in placing several reference spheres on the rock blocks when the fracture was closed. Next, the relative position between the spheres was scanned. Then, the sample was opened and the two fracture surfaces, together with its respective reference spheres, were scanned separately. The final stage was accomplished by means of relocating the relative position of the reference spheres to their original position with high accuracy, obtaining the aperture values. Figure 3.1 shows the 3D isometric views of the digital replicas of the fracture obtained before and after relocation takes place.

Once the initial aperture map was defined, both translational and rotary shear were simulated independently using the digital replicas (Koyama *et al*., 2004; 2005). With regard to translational shear, the upper surface was progressively displaced tangentially with a 1 mm interval, simulating this shear process without normal loading, up to a total shear displacement of 20 mm. When the shear simulation starts, the digital images of the upper and lower surfaces of the sample were superimposed with a few contact (at least three) points. For each shear displacement step, the aperture map and contact area were calculated. As for the rotary shear, a similar method was utilized, but in this case the upper surface rotated around the lower one at 0.5^{o} shear angle intervals up to 90^{o} without considering normal loading and asperity degradation. Both processes can be viewed in Figure 3.2.

These two shearing processes are completely different, as it can be seen from Figure 3.2. During translational shear displacement, all the asperities of the upper surface were uniformly deformed or damaged along the shear direction. On the other hand, in the rotary shearing process, the shear displacement is non-uniform, due to the fact that the closer the asperities are to the rotary centre, the smaller the displacement they experience.

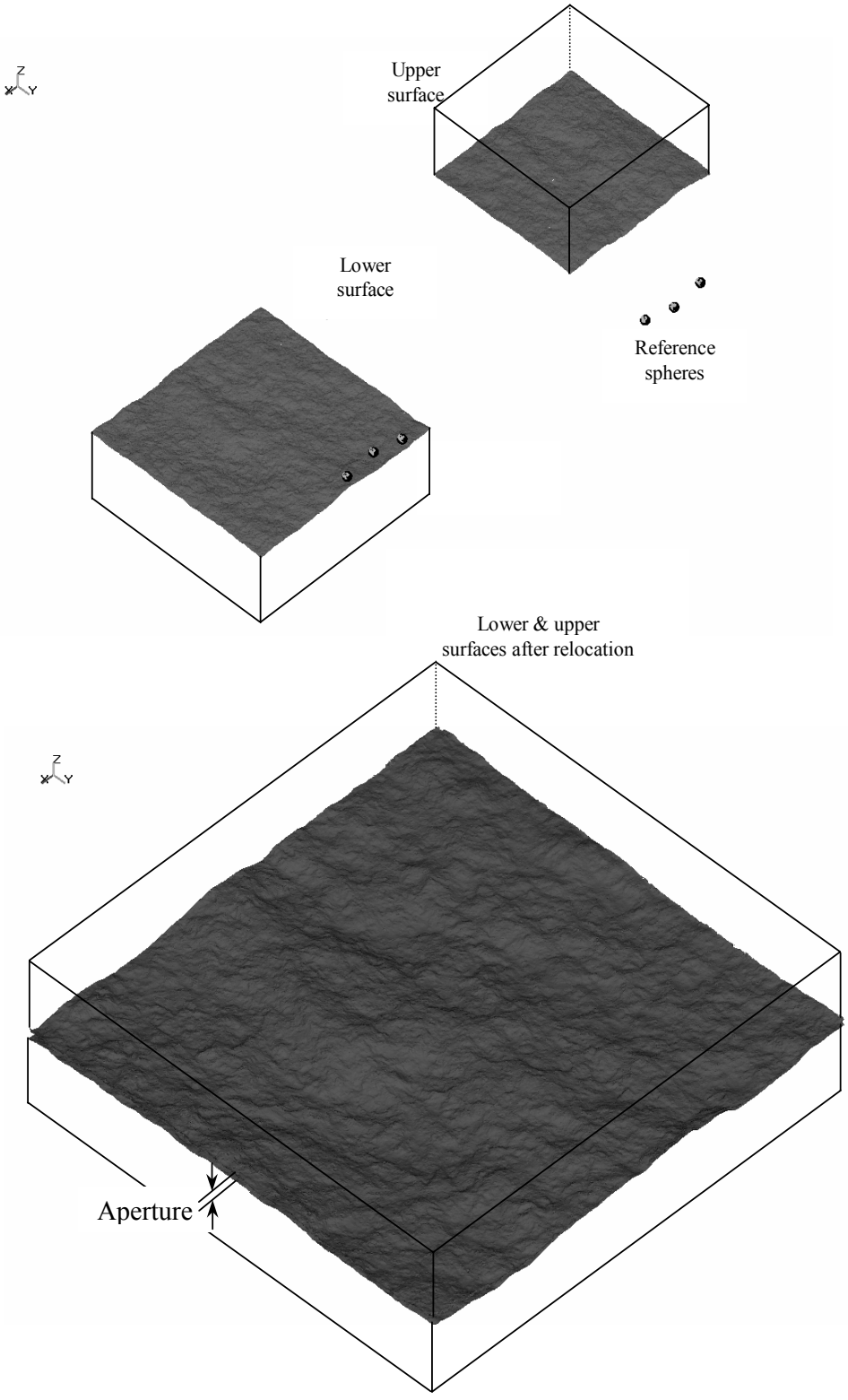

Figure 3.1. 3-D isometric views of the digital replicas (from Koyama et al., 2005).

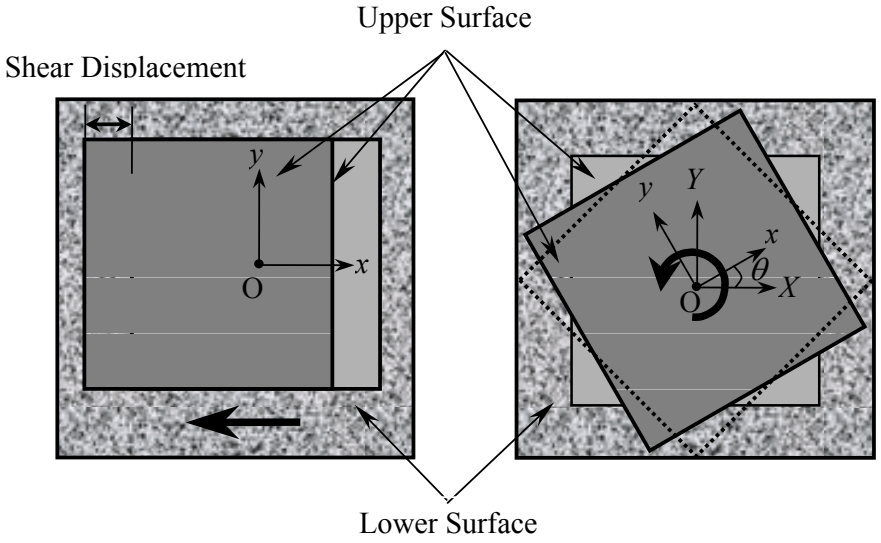

Figure 3.2. The translational and rotary shearing processes.

To guarantee a constant overlap between the lower and the upper fracture surfaces during shear, the size of the upper block was reduced. While the size of the lower surface was fixed, with a size of 250x250 mm, the upper surface, which was moved along the lower surface during the shearing processes, adopted two different sizes depending on the shearing process. As far as translational shear is concerned, the size of the upper surface was 194x194 mm, so that there was a complete overlap between the two surfaces during the 20 mm shear displacement. With regards to the rotary shear, the upper surface had a size of 136x136 mm, allowing a rotation of 90 degrees with a complete overlap during the whole process.

Nevertheless, this study considered only a rotary shear up to 10 degrees. The reason for this limitation lies on the conclusions drawn by Koyama *et al*. (2004), and because usually there can only be found small rotary shear displacements in natural fractures. Koyama *et al*. (2004) stated that the aperture would increase drastically for small rotary shear, but for larger values the increase rate would become almost constant. Related to this finding, it was found that, with increasing the rotary shear angle, the flow rate would increase sharply at the start of the shearing process, but then would become almost constant for larger rotary shear angles. Furthermore, the flow patterns during rotary shear would become isotropic rapidly. Overall, significant changes in results would come from the shearing process for small rotary angles.

Taking the previously mentioned points into account, the following criterion was followed in order to choose an appropriate upper limit for the rotary angle. As the translational shear had a maximum displacement of 20 mm, the same displacement was considered for the most distant point from the rotary axis, i.e. one of the corners of the 136x136 mm rough fracture sample. This corresponds to an angle of almost 12 degrees, which was rounded down to 10 degrees.

3.2. CHARACTERIZATION OF SURFACE ROUGNESS USING GEOSTATISTICAL APPROACH

In this study, spatial correlation was quantitatively studied using semi-variograms. The importance of this geostatistical approach lies on the possibility that it offers to study the directional and scale behaviour of the rough fracture during shear. A semi-variogram shows the variation between pairs of data as a function of the distance between them, i.e. lag distance. Fardin (2003) used a fractal approach to characterize the surface roughness of the fracture, however no quantitative evaluation of anisotropy of the aperture and transmissivity distributions was considered. For this reason, the use of semi-variograms was chosen for the current study. Semi-variogram analysis was carried out using a code from GSLIB (Deutsch et al., 1998).

Semi-variograms represent semi-variance versus lag distance. The semi-variance $\gamma(l)$ is defined as

$$\gamma(l) = \frac{1}{2}\mathrm{E}\left[\left(z(\mathbf{x}) - z(\mathbf{x}')\right)^2\right] \tag{1}$$

$$l = \left\|\mathbf{x} - \mathbf{x}'\right\| \tag{2}$$

where l is the lag distance, $z(\mathbf{x})$ is the variable of interest taken at location x and $z(\mathbf{x}')$ is the variable of interest taken at a point $\mathbf{x}'$ from a distance of l away. The lag distance indicates the distance between the pair of points that are compared. When large values of $\gamma(l)$ are obtained, it means that the parameter of interest is not correlated for the selected l distance. Nevertheless, for experimental studies, where a significant number of measurements have been done, it uses the following formulation

$$\gamma(l) = \frac{1}{2N(l)}\sum_{i=1}^{N(l)}\left[z(x_i) - z(x_{i+l})\right]^2 \tag{3}$$

where $N(l)$ is the number of observations pairs for a given lag distance l as defined above. The semi-variance increases with increasing lag distance up to a certain point, and then it becomes constant. This plateau level of a semi-variogram is known as a sill, and the lag distance at which the semi-variogram reaches the sill is called range or spatial correlation length, as it can be seen in Figure 3.3.

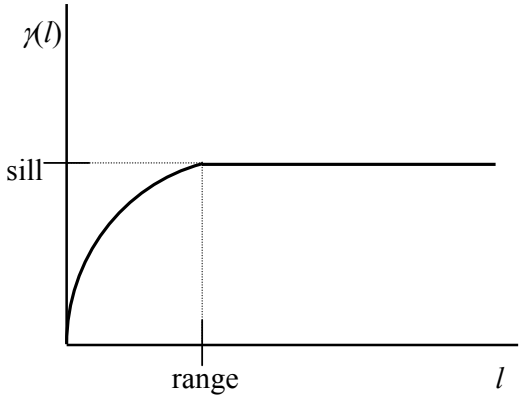

Figure 3.3. Outline of a semi-variogram, indicating its range and sill.

The correlation length is a measure of how abruptly the aperture changes along the rough fracture. For instance, long correlation length will have fewer, but larger, contact areas, resulting in fewer channels through which fluid will flow, as compared to fractures with shorter correlation length (Hakami *et al*., 1995). In addition, the larger the contact area is, the larger the range becomes. As reported in Hakami *et al*. (1996), simply knowing the aperture frequency distribution is not enough, because despite the fact that the aperture frequency distribution of two fractures may be very similar, their spatial correlation length can be significantly different, resulting in different hydro-mechanical characteristics. Furthermore, for an anisotropic void geometry, the range and/or the sill differ depending on the considered direction on the fracture surface (Hakami *et al*., 1995). Apart from this, it may be interesting to describe the calculated experimental semi-variograms by fitting the curve to a semi-variogram model, specially if spatially correlated stochastic variables need to be generated (Hakami *et al*., 1996).

Lastly, some interesting results concerning the shear effects on the aperture frequency distribution are found by Yeo *et al*. (1998). After a translational shear, up to 2.0 mm, occurs, the direction perpendicular to the shear direction is found to be more correlated than the direction parallel to the shear displacement due to the channelling. Similar results were also reported in the study carried out by Koyama *et al*. (2005) using fractal analysis, but are not quantified using this geostatistical approach, i.e. semi-variogram analysis. In this study, both the aperture value and the transmissivity have been studied using semi-variograms. For the case of the transmissivity, due to the fact that its range of values is very wide, the study was carried out using de logarithm in base 10 of the transmissivity.

3.3. NUMERICAL METHODS

3.3.1. FLOW CALCULATION USING FEM

As introduced in the previous sections, the geometry of a rock fracture, i.e. roughness and void volume, is far from uniform and it changes during shear processes. Surely, shear induced anisotropy and heterogeneity in the aperture values will affect fluid flow behaviour. Due to its flexibility, a numerical simulation has been applied to study different flow patterns and boundary conditions through the digitalized rough rock fracture, using a finite element method for the resolution of the Reynolds equation for flow through single rock fracture (Koyama *et al*., 2004, 2005).

The numerical modelling developed for this study, solved the Reynolds equation using a finite element code. The Reynolds equation describes flow between slightly non-planar and non-parallel surfaces (Brown, 1987). When flow rate is low and the aperture does not vary too abruptly the Reynolds equation is applicable, instead of the full Navier-Stokes equation, to describe steady flow in fractures (Zimmerman *et al*., 1991, 1996; Yeo *et al*., 1998). Considering steady state flow of an incompressible fluid and assuming that the flow follows the cubic law, the governing equation can be written as

$$\frac{\partial}{\partial x}\left(T_{xx}\frac{\partial h}{\partial x}\right)+\frac{\partial}{\partial y}\left(T_{yy}\frac{\partial h}{\partial y}\right)+Q=0 \qquad (4)$$

where Q is the source/sink term, taken to be positive if fluid is flowing into the fracture and negative if fluid is flowing out of the fracture, and T_{xx} and T_{yy} are, respectively, the fracture

transmissivity in the *x*- and *y*-directions. In this study, for simplicity, the local transmissivity at each point is assumed to have the same value in both *x*- and *y*-directions, being defined as

$$T_{xx} = T_{yy} = T(x, y) = \frac{\rho_f g b^3}{12\mu} \tag{5}$$

where μ is the dynamic viscosity, ρ_f the fluid density, g the gravitational acceleration, and b the local fracture aperture. The flow of the single rock fracture is simulated using FEM. This FEM code requires the local transmissivity of the fracture, which is different from element to element, varying according to the aperture values obtained in each shearing stage. For the calculations, the density and the dynamic viscosity of water at 20°C were used. That is to say, $\rho_f = 9.982 \times 10^2\ kg/m^3$ and $\mu = 1.002 \times 10^{-3}\ Pa \cdot s$. As for the gravitational acceleration, its value was taken as $g = 9.807\ m/s^2$.

Applying the Galerkin method to the Eq. (4), the discretized governing equation can be written as

$$\sum_{m=1}^{N} \left[K^{(m)}\right] \left\{h^{(m)}\right\} = \sum_{m=1}^{N} \left\{F^{(m)}\right\} \tag{6}$$

with

$$\left[K^{(m)}\right] = \int_{S^{(m)}} \left[B^{(m)}\right]^{\mathrm{T}} \left[D^{(m)}\right] \left[B^{(m)}\right] dS \tag{7}$$

$$\left\{F^{(m)}\right\} = \int_{S^{(e)}} \left[N^{(m)}\right]^{\mathrm{T}} Q^{(m)} dS - \int_{L^{(m)}} \left[N^{(m)}\right]^{\mathrm{T}} \left(T \frac{\partial h}{\partial x} n_x + T \frac{\partial h}{\partial y} n_y \right) dL \tag{8}$$

where N is the total number of elements, m is the element number, and $[K^{(m)}]$, $\{h^{(m)}\}$, $\{F^{(m)}\}$, $[N^{(m)}]$, $S^{(m)}$ and $L^{(m)}$ are the local transmissivity matrix, the hydraulic head vector, the flux vector, the shape function matrix, the surface area and the boundary in the flow rate is known for element m, respectively. The unit normal vector components to the boundary in *x*- and *y*-direction are respectively symbolised by n_x and n_y. The matrices $[D^{(m)}]$ and $[B^{(m)}]$ are defined as follows

$$\left[D^{(m)}\right] = \begin{bmatrix} T & 0 \\ 0 & T \end{bmatrix} = \begin{bmatrix} \dfrac{\rho_f g b^{(m)3}}{12\mu} & 0 \\ 0 & \dfrac{\rho_f g b^{(m)3}}{12\mu} \end{bmatrix} \tag{9}$$

$$\begin{Bmatrix} i_x \\ i_y \end{Bmatrix} = \begin{Bmatrix} \dfrac{\partial h}{\partial x} \\ \dfrac{\partial h}{\partial y} \end{Bmatrix} = \begin{Bmatrix} \dfrac{\partial \left[N^{(m)}\right]^{\mathrm{T}}}{\partial x} \\ \dfrac{\partial \left[N^{(m)}\right]^{\mathrm{T}}}{\partial y} \end{Bmatrix} \left\{h^{(m)}\right\} = \left[B^{(m)}\right] \left\{h^{(m)}\right\} \tag{10}$$

The FEM code used in this study uses linear quadrilateral elements to solve Eq. (6) (Koyama *et al*., 2005). For this purpose, the local transmissivity value was calculated using the average aperture value in each element, as shown in Figure 3.4. Thus, in order to simulate the fluid flow through the fracture during both shear processes, the transmissivity of each element was evaluated at each shear displacement using Eq. (5).

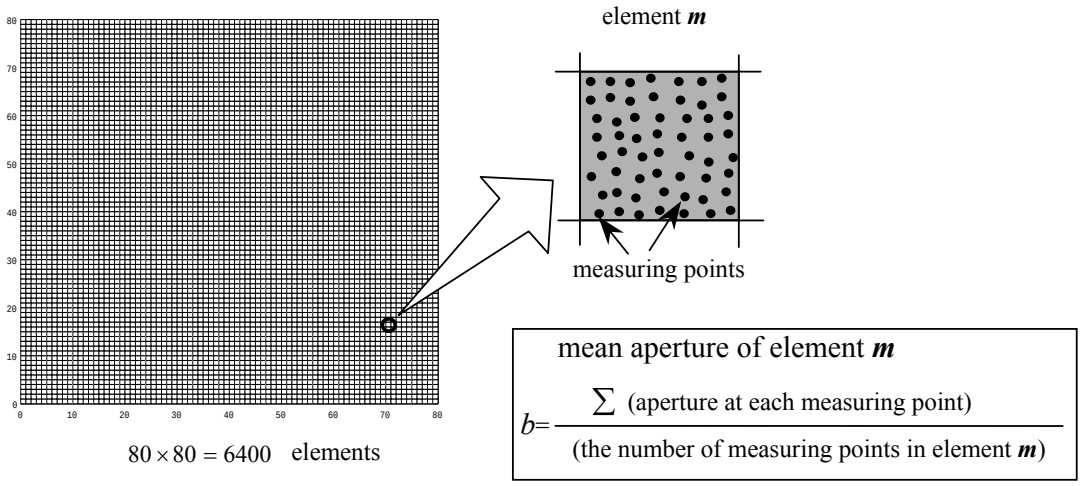

Figure 3.4. Calculation of the mean aperture for each element.

A numerical simulation needs representation of the natural rough fracture in a regular mesh in which the governing equations can be solved element by element. For this study, a regular rectangular mesh of 80x80 elements was generated, resulting in 6,400 elements. Thus, in the translational shear case, with a fracture size of 194x194 mm, each element had a side length of around 2.5 mm. As for the rotary shear, in which the fracture size was of 136x136 mm, the side of each element was of 1.7 mm. In order to determine the aperture, which is crucial for the success of the study, the two 3D-laser scanned surfaces of a rock fracture were superposed and an aperture map was generated. Next, the aperture value of an element was calculated as an average of all the apertures values available in the aperture map that correspond to that element, as it can be seen in Figure 3.4.

In this study, different fluid flow situations are considered. For the translational shear, three different flow patterns - unidirectional, bi-directional and radial - have been taken into account. For rotary shear only the radial flow pattern has been taken into consideration. As for unidirectional flow, the two possible situations, i.e. flow parallel and perpendicular to the

shear direction, were studied. Due to experimental limitations, specially the fluid sealing difficulty, laboratory coupled shear-flow experiments can only reproduce reliably flow tests in the direction parallel with shear displacement (see Figure 3.5). Nevertheless, Yeo *et al*. (1998) developed an experimental apparatus with which they carried out a test with fluid flowing perpendicular to the shear displacement. Interestingly, a channelling phenomenon appears during shear displacement in the direction perpendicular to the shear direction, allowing a greater quantity of fluid to flow along this direction rather than in the direction parallel with shear (Gentier *et al*., 1996; Yeo *et al*., 1998; Mitani *et al*., 2002; Jing *et al*., 2004; Kim *et al*., 2004; Koyama *et al*., 2005). Using numerical simulation, this channelling phenomenon can now be identified and studied in detail. Apart from this, a more realistic interpretation of the flow conditions that can be found under general fracture deformation modes can now be carried out by means of defining a bi-directional flow pattern. It should be noted that no experimental works of this kind of flow pattern has been done so far. The last flow pattern taken into consideration is radial flow, in which translational and rotary shear were compared. This last approach can also be reproduced in laboratory. The effects on radial flow during translational shear in a rectangular sample have been studied by Esaki *et al*. (1995a, 1995b, 1999), Yeo *et al*. (1998) and Mitani *et al*. (2002). Unlike translational shear, radial flow tests under rotary shear can only be performed in the laboratory with hollow cylinder samples, due to the geometrical difficulties of applying a rotary torque in a rectangular specimen (Olsson, 1992; Olsson *et al*., 1993; Cheon *et al*., 2002).

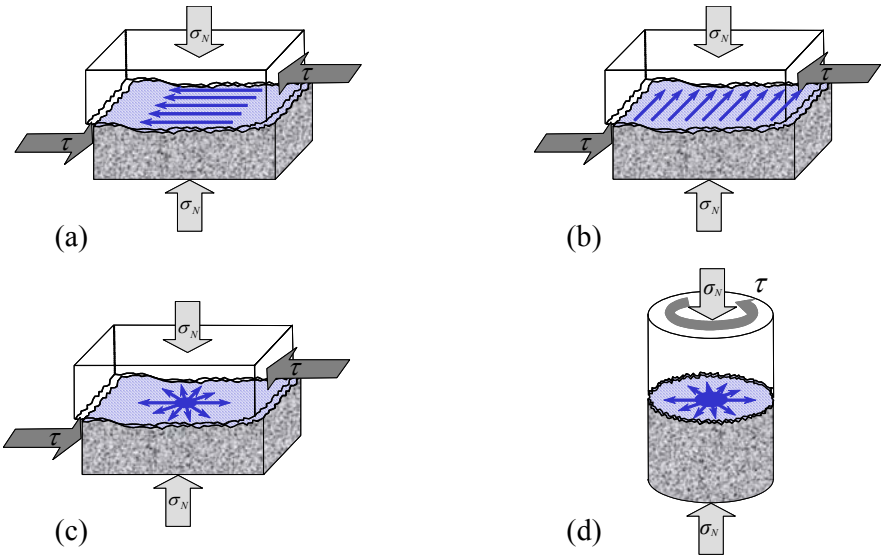

Figure 3.5. Different experiments (a) flow parallel to shear direction, (b) flow perpendicular to shear direction, (c) radial flow under translational shear and (d) radial flow under rotary shear.

In this study, the boundary conditions were defined according to the flow patterns. In Figure 3.6 an outline of the flow boundary conditions for each particular situation is shown. As for the unidirectional flow, when flow was parallel to shear direction, the upper and lower boundaries did not permit any flow through them. While the right-hand boundary had a hydraulic head of 1.0 m, the left-hand boundary had a 0.0 m hydraulic head. As for the flow perpendicular to shear direction, the same boundary conditions applied, but rotated 90 degrees in the clockwise direction. As far as bi-directional flow is concerned, the lower and the right-hand boundaries had a hydraulic head of 1.0 m, and the other two boundaries had a 0.0 m

hydraulic head. Finally, radial flow patterns had a head drop of 1.0 m, with a hydraulic head of 1.0 m in the centre, and 0.0 m hydraulic head in the outer boundaries.

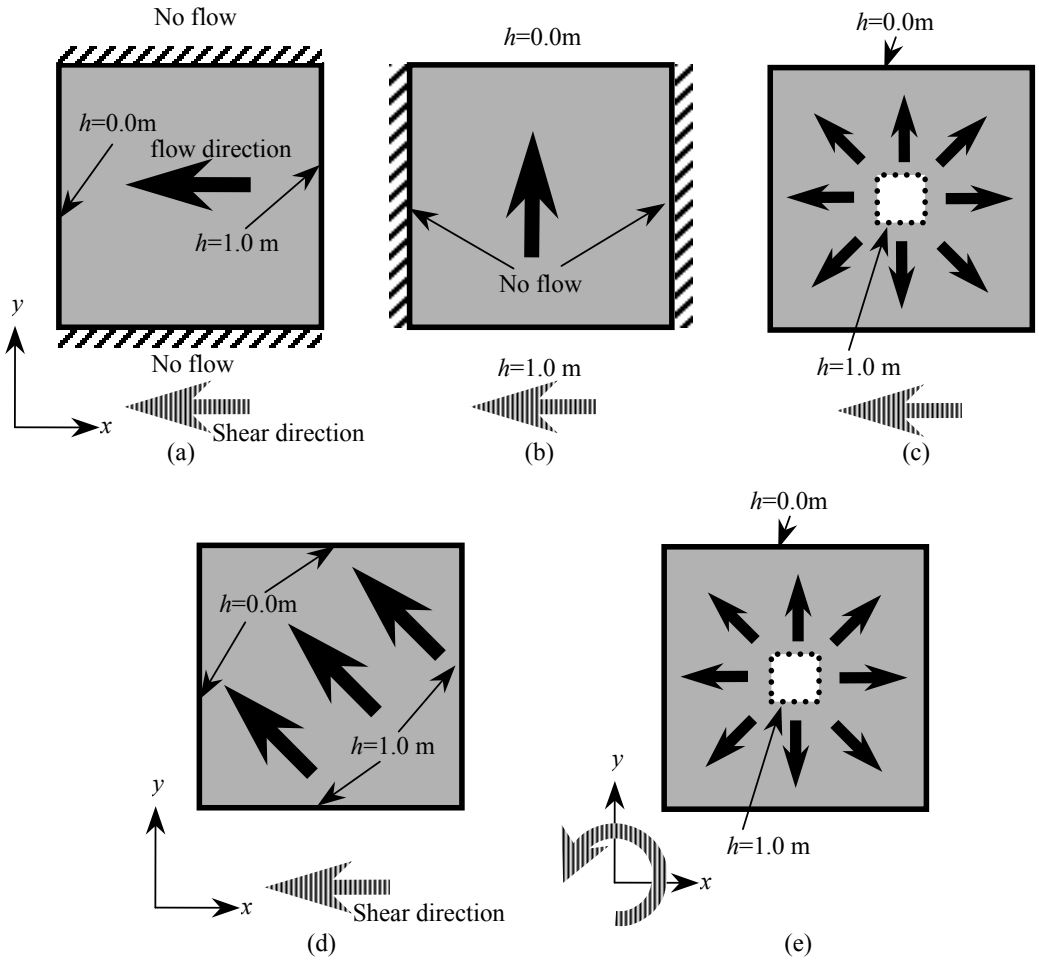

Fig. 3.6. Different combinations of flow boundary conditions and shearing processes. Unidirectional flow pattern, (a) parallel and (b) perpendicular to the translational shear, (d) Bi-directional flow pattern with translational shear and Radial flow pattern under (c) translational and (e) rotary shear.

3.3.2. PARTICLE TRACKING ALGORITHM

Particle transport in rough rock fractures is a highly interesting topic that has been studied extensively before by several researches using a numerical approach (Neretnieks *et al*., 1982; Moreno *et al*., 1988, 1990, 1991; Cvetkovic *et al*., 1999; Cheng *et al*., 2003; Tsang *et al*., 2003). Field experiments are very rare and expensive, and the results are sometimes quite difficult to be properly evaluated (Abelin *et al*., 1991a, 1991b). The experimental limitations in laboratory coupled shear-flow tests for direct observation of paths that particles will follow indicate that the numerical simulations may be a more powerful tool. In this study, an approach to particle tracking has been developed, in which the particles followed the flow velocity field, considering only advection.

Regarding laboratory experiments, however, a recent research conducted by Jiang *et al*. (2004), allows the visualization of particle transport at laboratory during direct shear-flow test. A color camera was placed above the shear-flow test apparatus, taking photos at specific intervals after a tracer flow was injected into the fracture. A transparent epoxy replica was used, so that flow process during shear flow tests can be studied. Nevertheless, in order to perform this experiment, the stiffness of the apparatus is reduced greatly. Furthermore, with a numerical approach, a wider range of boundary conditions can be simulated compared to laboratory tests.

Before describing the algorithm for particle tracking, a theoretical approach is needed in order to understand the whole process. The advection-dispersion equation can be written as

$$R\rho\theta\frac{\partial c}{\partial t}=\frac{\partial}{\partial x_i}\left(\rho\theta D_{ij}\frac{\partial c}{\partial x_i}\right)-\rho\theta V\frac{\partial c}{\partial x_i}-R\rho\theta\lambda c+Q_c \qquad (11)$$

where c is the volumetric concentration, R is retardation coefficient [$M^{-1}L^3$], ρ is the fluid density [ML^{-3}], θ is the volume water content, t is time [T], D_{ij} is dispersion tensor [L^2T^{-1}], V is the real velocity [LT^{-1}], λ is the radioactive decay coefficient [T^{-1}], and Q_c is the source/sink term. The coefficients R and λ satisfy that they are greater or equal to 0, and D_{ij} is a symmetric positive-semidefinite tensor.

This equation can be solved directly using a Eulerian method, using a fixed grid and a finite difference approach. Nevertheless, this method is very unstable and some restrictions are imposed by the Péclet number in the grid size and the Courant number in the time step in order to reduce the instabilities and guarantee the convergence of the solution.

Another possibility consists in solving the equation by means of Lagrangian methods, which require a deforming grid or a fixed grid with deforming coordinates. This method is convenient when advection is dominant in front of dispersion.

A third approach, Eularian-Lagrangian method, consists in assuming that the volumetric concentration can be divided into two parts, one related to advection $\bar{c}$ and the other to dispersion $\tilde{c}$.

$$c(x_i,t)=\bar{c}(x_i,t)+\tilde{c}(x_i,t) \qquad (12)$$

Then, the advection-dispersion equation, Eq. (11), can be perfectly decoupled into two independent problems, a purely hyperbolic "advection problem" defined in terms of $\bar{c}$, Eq. (13), and a predominantly parabolic "dispersion problem" defined in terms of $\tilde{c}$, Eq. (14) (Neuman, 1984). This approach, which is very convenient when advection is dominant, combines the Lagrangian form with the Eularian form, presenting very few limitations, due to the fact that it can handle the entire range of Péclet numbers from 0 to ∞, with Courant numbers greatly exceeding 1 (Neuman, 1984). In other words, the decoupling of Eq. (11) eliminates Courant number restrictions and provides and effective way of dealing with very different time scales.

$$\frac{d\bar{c}}{dt}=\frac{\partial c}{\partial t}+\frac{V_i}{R}\frac{\partial c}{\partial x_i}=-\lambda\bar{c} \qquad (13)$$

where V_i is the real velocity.

$$R\rho\theta\frac{d\tilde{c}}{dt}=\frac{\partial}{\partial x_i}\left(\rho\theta D_{ij}\frac{\partial c}{\partial x_i}\right)-R\rho\theta\lambda\tilde{c}+Q_c \tag{14}$$

A more detailed development with the steps to decouple the advection-dispersion equation in found in Appendix A.

In the present study, the first approach to particle transport has been considered, considering only the advection problem and ignoring dispersion, sorption or radioactive decay. It has to be noted that the interest of this study lies on gaining knowledge about the behavior of particle transport in a rough fracture during mechanical shear, which has never been done before, and therefore requires firstly a straightforward and much simplified approach.

From the advective problem, considering $\lambda=0$, the new position of a particle *j* in the iteration *i+1* is given by

$$x_j^{i+1}=x_j^i+\int_{t^i}^{t^{i+1}}\frac{V}{R}dt \tag{15}$$

where x_j^{i+1} is the position of the particle *j* after the iteration *i+1* and x_j^i is the position of the particle *j* in iteration *i*. In this case, *R*=1, and solving the integration, one can obtain the mean value of the velocity $\overline{V}$ for a certain element under study. Therefore, the increment of time in each iteration can be calculated as follows:

$$\Delta t=\frac{x_j^{i+1}-x_j^i}{\overline{V}} \tag{16}$$

In order to conduct this experiment, a numerical approach capable of tracking the introduced particles at different initial position under different flow boundary conditions has been developed using Matlab. The numerical approach, considering a steady state problem, consists of six subroutines, and the main algorithm consists of three steps. The code was adapted for each particular boundary condition, but the structure remains the same for all the cases. The subroutines are described bellow.

1) Reading in the input data, generating a FEM mesh and solving the fluid problem for velocity field in the fracture;
2) Determining the initial position of each particle in the relevant element;
3) Running of the algorithm for every flow patterns for:
    a. Calculation of the particle's position at each iteration;
    b. Calculation of the travel distance and travel time at each iteration;
    c. Calculation of the relative position for the next iteration;
4) Identifying the number of iterations required for each particle;
5) Calculating travel time, travel distance and tortuosity for each particle;
6) Plotting the numerical results.

In the main algorithm, the simulation continues until the particle reaches a pre-specified outflow boundary, and then, it jumps to the next particle. The loop is repeated as many times as number of particles are introduced in the fracture. The particles move parallel to the corresponding element's velocity vector in each iteration. In order to make it clearer, figure 3.7 shows a flowchart of the functioning of the code.

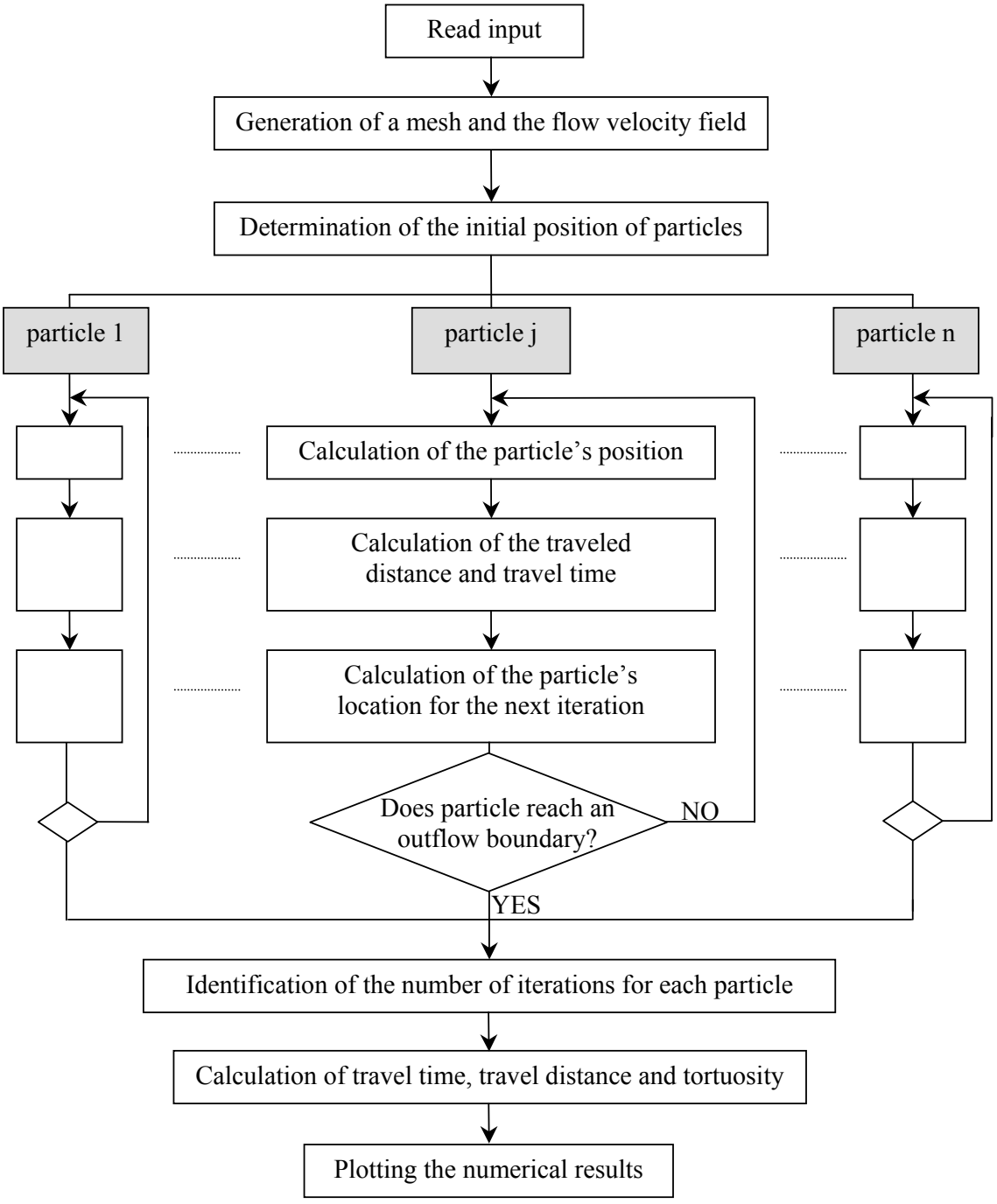

Figure 3.7. Flowchart of the functioning in the particle tracking code.

The movement inside the elements follows the velocity vector of each element, which is defined by its magnitude and the angle with respect to the *x*-coordinate axis. As mentioned before, the elements are squares of a side length of *L*. *L* can take two values, 2,5 mm for the translational shear and 1,7 mm for the rotary shear. The increment in the position of the particle in the *x* and *y*-directions in every iteration is given by the conditions inside the element. For instance, Figure 3.8 depicts two particular cases, one in which the particle advances *L* in the *y*-direction, and $L/\tan\theta$ in the *x*-direction, where θ is the angle that form the velocity vector with the *x*-coordinate; and in the other one the particle advances *L* in the *x*-direction and $L \cdot \tan\theta$ in the *y*-direction. There are other possible situations, which can be easily solved using trigonometry.

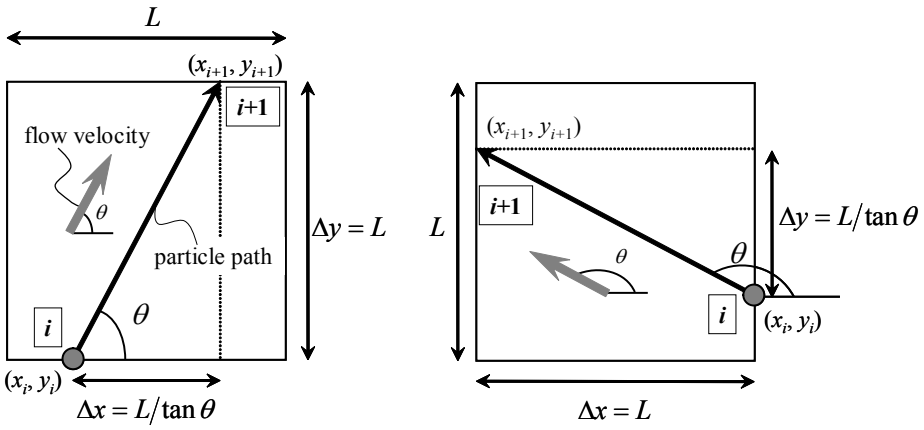

Figure 3.8. Typical particle movement from iteration *i* to *i*+1 following flow the velocity vector in a certain element for two different situations.

In order to illustrate the criterion chosen for the particle tracking algorithm, a simplified mesh of 9 elements is shown in Figure 3.9. Usually, the velocity vector has similar velocity components for adjacent elements. That is to say, if the velocity vector of one element is pointing to the upper right direction, the velocity vector of its neighbour will point in the same direction, varying slightly, in direction and magnitude, as it is shown for particle number 1 in Figure 3.9. Nevertheless, there are some situations in which a particle hits an element of its neighbour with such a velocity vector that provokes the particle changing its direction, as can be seen in the central element for particle number 2 in Figure 3.9. In such cases, the particle follows the velocity vector of the corresponding element for a particular iteration, though its track does not pass through the mentioned element, because the velocity vector points out in the opposite direction that the particle was coming from. As far as the particle number 2 in Figure 3.9 is concerned, in the first iteration it follows a direction parallel to the velocity vector of its starting element, and hits the central element. In the next iteration, the particle follows the velocity of the central element, and hits the element that is placed to the right in the central row. The velocity vector of this element points to the top left-hand side direction, and therefore, particle 2 will follow this direction. Therefore, traveling through the central element, it hits the central element of the top row. Finally, particle 2 hits the element placed in the top right-hand corner and afterwards reaches an outflow boundary. As for particle number 3, the directions of the elements it passes changes, but unlike particle 2, it hits them in a way that always travels through the corresponding element in every iteration. Apart from this, it has to be noted that the length of the velocity vectors, in blue, in Figure 3.9 is directly proportional to its magnitude.

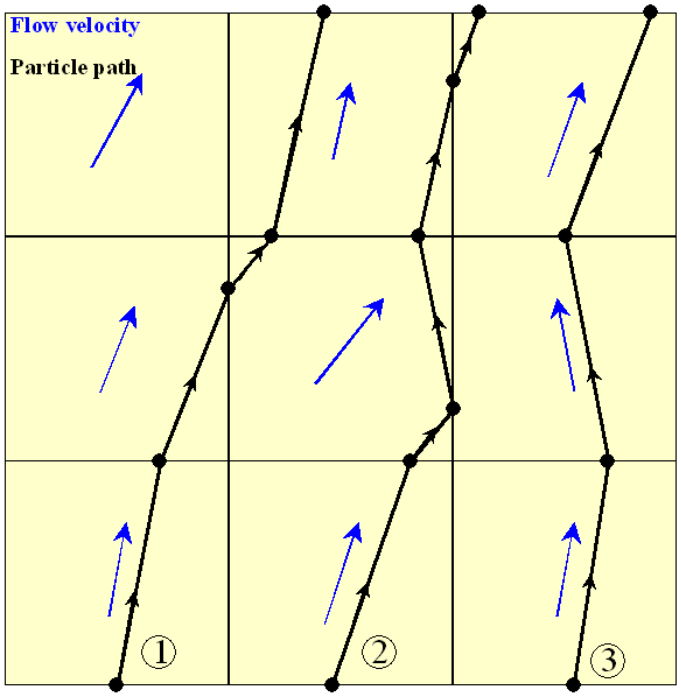

Figure 3.9. Outline of particle tracking using a mesh of 3x3 elements.

As input data, the fluid flow velocity field is given from flow calculations. Thus, the residence time in each element has been calculated from the traveled distance in each element and its corresponding velocity, as shown in Eq. (16). As for the particle travel time, it is calculated as the sum of the residence time of all the elements each particle goes through (Eq. 17). Similarly, the travel distance is calculated as the sum of all the travel distances inside each element (Eq. 18).

$$t_j = \sum_{i=1}^{m} t_j^i \qquad (17)$$

where t_j is the travel time of particle j, t_j^i is the time of particle j in iteration i and m is the number of iterations made by particle j.

$$d_j = \sum_{i=1}^{m} d_j^i \qquad (18)$$

where d_j is the travel distance of particle j, d_j^i is the travelled distance of particle j during iteration i and m is the number of iterations made by particle j.

As far as the tortuosity is concerned, it has only been considered in the unidirectional flow patterns, and it has been assumed to be the quotient between the travel distance and the theoretical distance that the particle would travel if the aperture value of the fracture would be constant, i.e. in a parallel plate fracture. In the parallel plate fracture model, the flow is

uniform, and therefore, the particles would follow straight lines, being its travel distance equal to the fracture side, which in this case is equal to 194 mm. If the distance traveled by particle *j* is called d_j, the tortuosity is given by Eq. (19).

$$tort_j = \frac{d_j}{d_L} = \frac{d_j}{194} \tag{19}$$

where $tort_j$ is the tortuosity of particle *j* and d_L is the length of the fracture. It has to be noted that this parameter is dimensionless and its values are greater than 1, due to the fact that the particles will follow meandrous paths longer than the fracture length. Although this definition of tortuosity could also be valid for the bi-directional and the radial flow, as they imply a more complicated flow pattern, it was thought that the interpretation of the results would be too ambiguous and cumbersome to be included in this study.

As for the number of particles, it was considered that a fair approach would be to introduce as many particles as the number of elements that form a side of the sample, i.e. 80 particles. As far as the unidirectional flow is concerned, it was thought that one particle in each element of the inflow boundaries would be representative of that element, and that given the case that two particles were placed in the same starting element, it would give repetition in results. Regarding the bi-directional flow patterns, in order to maintain the number of particles of the unidirectional flow, half of the particles were placed in each inflow boundary, that is to say 40 particles in the lower boundary and 40 particles in the right hand boundary. With regards to the radial flow pattern, as the central hole was very small, 6x6 elements, it seemed sensible to introduce two particles in each inflow element, thus making a total of 48 particles. Despite the fact that for the unidirectional and bi-directional flow patterns the calculations of particle travel time and tortuosity were made using 80 particles, the presentation of the results in this thesis has been done using 50 particles in order to make it clearer. In all the cases the particles were placed equidistantly.

The results that were obtained from Matlab were the plots of the paths that particles followed in every single situation, their travel time and travel distance, from which tortuosity was calculated. For the analysis of the travel time, breakthrough curves were used in all cases, and in unidirectional flow histograms were also used. With the aid of these graphics, the evolution of the particle transport can be studied during the shearing processes, and it is also possible to compare different cases, such as flow parallel to shear direction and flow perpendicular to it in the unidirectional flow patterns. Moreover, the percentiles 10 %, 50 % and 90 % of the breakthrough curves are presented in tables, in order to make a quantitative analysis. These percentiles show the time at which the corresponding percentage of particles has arrived to an outflow boundary. As for the bi-directional flow patterns, the directional breakthrough curves, in *x*-direction and *y*-direction, were taken into account, as well as the total breakthrough curve, considering both outflow boundaries. With regards to the radial flow patterns, not only the directional breakthrough curves were taken into account, but also the breakthrough curves corresponding to each outflow boundary; as well as the breakthrough curve for the total number of particles. Furthermore, for the unidirectional flow a statistical analysis was carried out, calculating the mean travel time using Eq. (20), and its standard deviation using Eq. (21) for every shear displacement.

$$\bar{t} = \frac{1}{n}\sum_{j=1}^{n} t_j \tag{20}$$

$$\sigma_t = \sqrt{\frac{\sum_{j=1}^{n}(t_j - \bar{t})^2}{n-1}} \qquad (21)$$

where t_j is the travel time of particle j and n is the number of particles, which is equal to 80 for the unidirectional. As for tortuosity, histograms were used in order to analyze the difference in particle transport between the x-direction and the y-direction for unidirectional flow patterns during translational shear. This study was carried out to gain a better understanding of the shear induced channeling effect that is formed perpendicular to shear direction. However, for bi-directional and radial flow patterns, tortuosity was not considered, because the particles in these flow patterns follow not rectilinear paths, and furthermore, the paths that the particles followed during the shear processes are not similar to the paths that they follow in the parallel plate fracture. Therefore, the interpretation of the results would have been ambiguous and cumbersome.

For the presentation of the results, not all the cases have been shown, but rather some selected shear displacements and some selected rotary angles. The selected cases consist of the initial situation, before shearing, most of the cases at the starting shearing processes, and some of large shear displacements. The reason for this criterion has already been mentioned before. During the shearing processes, the most significant changes occur at small shear displacements; for large shear displacements, the changes are smaller. This selection of results was necessary in order to convey most of the information without going through all cases.